JOURNAL OF GEOPHYSICAL RESEARCH, VOL. 103, NO. B4, PAGES 7153–7169, APRIL 10, 1998

Mantle discontinuity structure beneath the Colorado Rocky Mountains and High Plains

Kenneth G. Dueker and Anne F. Sheehan

Cooperative Institute for Research in Environmental Sciences (CIRES) and Department of Geological Sciences, University of Colorado, Boulder

Abstract. Analysis of mantle discontinuity structure using converted P to S (P_dS) phases beneath Colorado from the Program for Array Seismic Studies of the Continental Lithosphere (PASSCAL) Rocky Mountain Front (RMF) experiment reveals significant topography at the 410 and 660 km depth discontinuities and corresponding transition zone thickness variations. A stack of all radial receiver functions resolves the 410 and 660 km discontinuities at average depths of 419 and 677 km, respectively. Imaging of lateral variations in mantle discontinuity structure is accomplished by geographically binning the P_dS conversion points and then stacking the receiver functions in each bin to form spatial images, analogous to common depth point stacking. Corrections for lateral velocity heterogeneity are calculated using the local S wave tomographic model of *Lee and Grand* [1996] and a constant $\partial lnV_S/\partial lnV_P$ scaling of 1.3. This scaling value is determined from the relative scaling between teleseismic P and S wave travel time residuals measured from the Rocky Mountain Front deployment. Mantle discontinuity images using 150 km square bins show 20 km of 410 km discontinuity topography, 30 km of 660 km discontinuity topography, and up to 40 km of transition zone thickness variation. Features of the discontinuity structure include a 20 km depression of the 660 km discontinuity beneath western Colorado and a gradual 10 km dip of the 410 km discontinuity beneath the High Plains. The thickening of the transition zone beneath southwest Colorado is consistent with the presence of the subducted Farallon slab in this region as imaged by *Van der Lee and Nolet* [1997]. In general, our results show that the transition zone discontinuity structure is more complex than that predicted by the simple model of olivine phase boundaries modulated by vertically coherent thermal anomalies.

1. Introduction

The occurrence of a rapid variation in velocity structure at a depth d (i.e., a seismic discontinuity) will produce three significant P to S converted phases: a transmitted P to S conversion (P_dS) and two topside reflection phases (Pp_dS and Ps_dS). In general, most research is focused on the P_dS arrival because the reverberations are less coherent due to their longer ray paths and increased timing sensitivity to dipping interfaces [e.g., *Cassidy*, 1992]. Accurate isolation of the converted arrivals provides a wealth of information regarding the depth, amplitude, and topography of the Earth's discontinuity structure [e.g., *Vinnik*, 1977; *Vinnik et al.*, 1983; *Paulssen*, 1988; *Shearer*, 1991; *Vinnik et al.*, 1996; *Gurrola et al.*, 1994; *Bostock*, 1996]. Together with mineral physics constraints [e.g., *Bina and Helffrich*, 1994], studies of mantle discontinuity structure help to illuminate the thermal and chemical structure of the mantle.

Accurate isolation of these small-amplitude P_dS arrivals can be difficult due to the presence of noise in the teleseismic P coda. Sources of signal-generated noise include scattering from surface basins [*Levander and Hill*, 1985] and nonplanar interfaces [e.g., *Clouser and Langston*, 1995]. With dense station coverage, receiver functions from multiple stations may be stacked together, providing significant improvement in the isolation of P_dS arrivals; coherent noise present at individual stations commonly becomes incoherent in multiple station stacks. In this study, we create common depth point stacks from a dense portable array of broadband seismometers in order to isolate P_dS arrivals.

The contribution of lateral velocity heterogeneity to P_dS timing variations must be accurately removed in order to image true discontinuity topography. From a global perspective, the correlation of $P_{410}S$ and $P_{660}S$ arrival times implies that lateral velocity heterogeneity above 410 km may dominate the timing of (P_dS) phases [*Stammler et al.*, 1992; *Bostock*, 1996; *Vinnik et al.*, 1996]. Therefore, without well-resolved local tomographic models from which P_dS timing corrections can be calculated, most previous research has resorted to measuring the transit time of a P_dS phase across the transition zone (subtracting the $P_{660}S$ times from the $P_{410}S$ times). Assuming relatively minor transition zone velocity heterogeneity [*Nolet et al.*, 1994], transition zone timing can be converted into relatively robust estimates of transition zone thickness variations. Assuming vertically coherent thermal structure throughout the transition zone, these P_dS transition zone thickness studies have been used to suggest that the thermal structure of the transition zone varies by less than 150 °C on average [*Stammler et al.*, 1992; *Bostock*, 1996; *Vinnik et al.*, 1996]. Other studies report larger transition zone thickness variations [e.g., *Gurrola*, 1995; *Flanagan and Shearer*, 1997].

Beneath the western United States, there is seismic evidence to suggest that the transition zone thermal structure is complex. The velocity structure above 300 km is very slow and heterogeneous [*Grand*, 1994; *Alsina et al.*, 1996; *Humphreys and Dueker*, 1994], and the transition zone contains high-velocity anomalies which may be associated with the Farallon slab [*Van der Lee and Nolet*, 1997]. We suggest that a structurally

Paper number 97JB03509.
0148-0227/98/97JB-03509$09.00

heterogeneous western U.S. transition zone results in 30 km transition zone thickness variations observed beneath the Yellowstone hotspot track [*Dueker and Sheehan*, 1997] and, as shown in this paper, now observed beneath the Rocky Mountain Front (RMF) array. Beneath the Yellowstone hotspot track, correlation of 410 and 660 km discontinuity topography was not found within the 600 km long sampling of the study. In this paper, we seek to quantify the transition zone thickness variations and any possible correlation between the 410 and 660 km discontinuities beneath the Colorado Rocky Mountains and High Plains.

2. Method

2.1. Data Set

The seismograms used in this study come from the Rocky Mountain Front PASSCAL (Program for Array Seismic Studies of the Continental Lithosphere) deployment of 25 broadband sensors in Colorado and western Kansas from June to November of 1992 (Figure 1). From this data set, 365 high-quality receiver functions are obtained by deconvolution of the vertical component P wave from the radial component [*Langston*, 1977]. The events used are from epicentral distances from 27° to 94°, and range in magnitude from 5.0 to 6.8. Before deconvolution, the traces are windowed from 10 s before to 120 s after the P wave arrival. Seismograms with clear PP arrivals are not used because of their different ray parameter with respect to direct P. The deconvolution is done using the spectral division technique with a water level parameter of 0.1 [*Clayton and Wiggins*, 1976]. After deconvolution, a second-order zero-phase Butterworth filter with band pass from 10-30 s is applied.

2.2. Binning of P_dS Ray Set

To form a three-dimensional image of the mantle discontinuity structure, the P_dS ray piercing points which intersect a plane at 530 km depth are geographically binned (Figures 1 and 2). The binning depth of 530 km is chosen because it is midway between the 410 and 660 km discontinuities, which are the focus of this paper. All rays within a bin are summed using move-out and lateral heterogeneity timing corrections to form a stack trace. Plotting all the stack traces sequentially creates an image of the mantle discontinuity structure, analogous to seismic reflection record sections. Both a global stack and stacks from 150 square km bins are performed.

2.3. Move-Out Corrections

Variations in source-receiver offsets result in systematic variations in P_dS arrival times, called move-out. To calculate the move-out of a P_dS phase, both P and S wave velocity models must be specified. We use the tectonic North America shear wave model TNA [*Grand and Helmberger*, 1984] with a V_P/V_S ratio of 1.84 [*Kennett and Engdahl*, 1991] for our move-out corrections. The arrival time of a P_dS arrival relative to the direct P wave in a flattened Earth is

$$T_{P_dS}(p) = \int_{-D}^{0} \left[\sqrt{V_S(z)^{-2} - p^2} - \sqrt{V_P(z)^{-2} - p^2} \right] dz \qquad (1)$$

where p is the P wave ray parameter in s/km and D is the depth of the discontinuity [*Gurrola et al.*, 1994]. The P_dS wave travels at the mantle shear velocity above the discontinuity with lag time behind direct P amounting to approximately 0.1 s per kilometer traveled. Thus 10 km of discontinuity topography will produce about 1 s of P_dS timing variation. The mapping of P_dS times to depth for vertically incident P wave ($p = 0$) is

$$T_{P_dS}(0) = \int_{-D}^{0} \frac{1}{V_S(z)} - \frac{1}{V_P(z)} dz \,. \qquad (2)$$

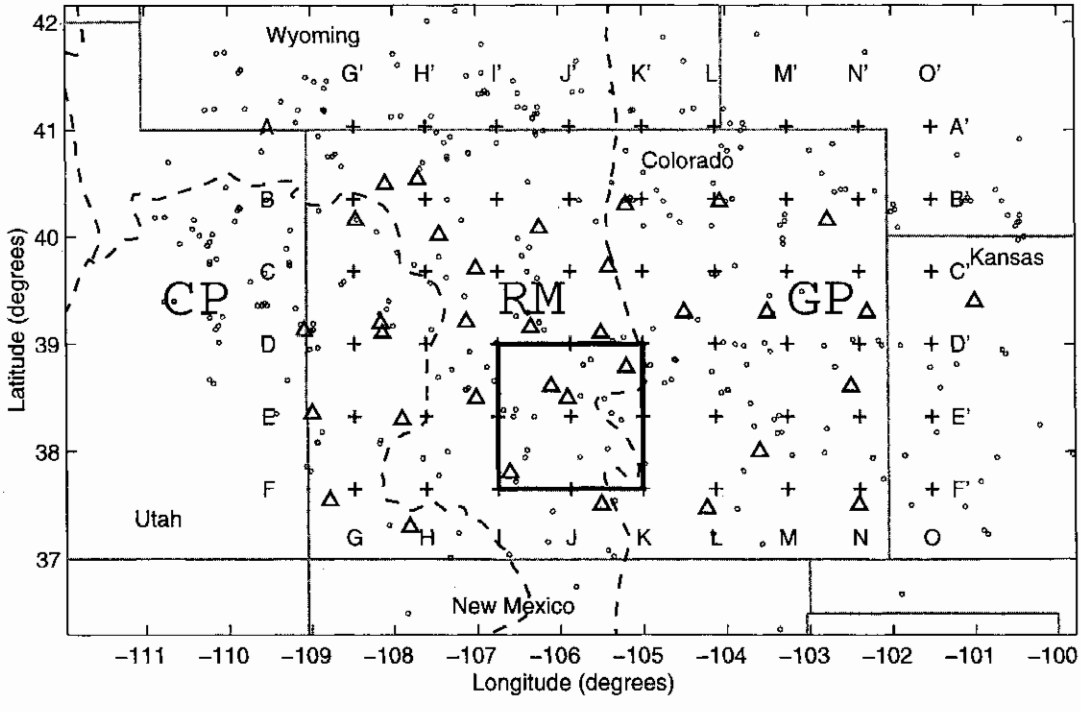

Figure 1. Seismograph stations of Rocky Mountain Front (RMF) PASSCAL experiment (triangles) and P_dS phase 530 km depth piercing points (small circles). Thin solid lines define state boundaries, dashed lines define physiographic provinces (CP=Colorado Plateau, RM = Rocky Mountains, GP = Great Plains). Center of 150 km square stack bins indicated by pluses, sample bin outlined by solid square in south central Colorado. A-A', B-B' etc. denote cross sections shown in later figures.

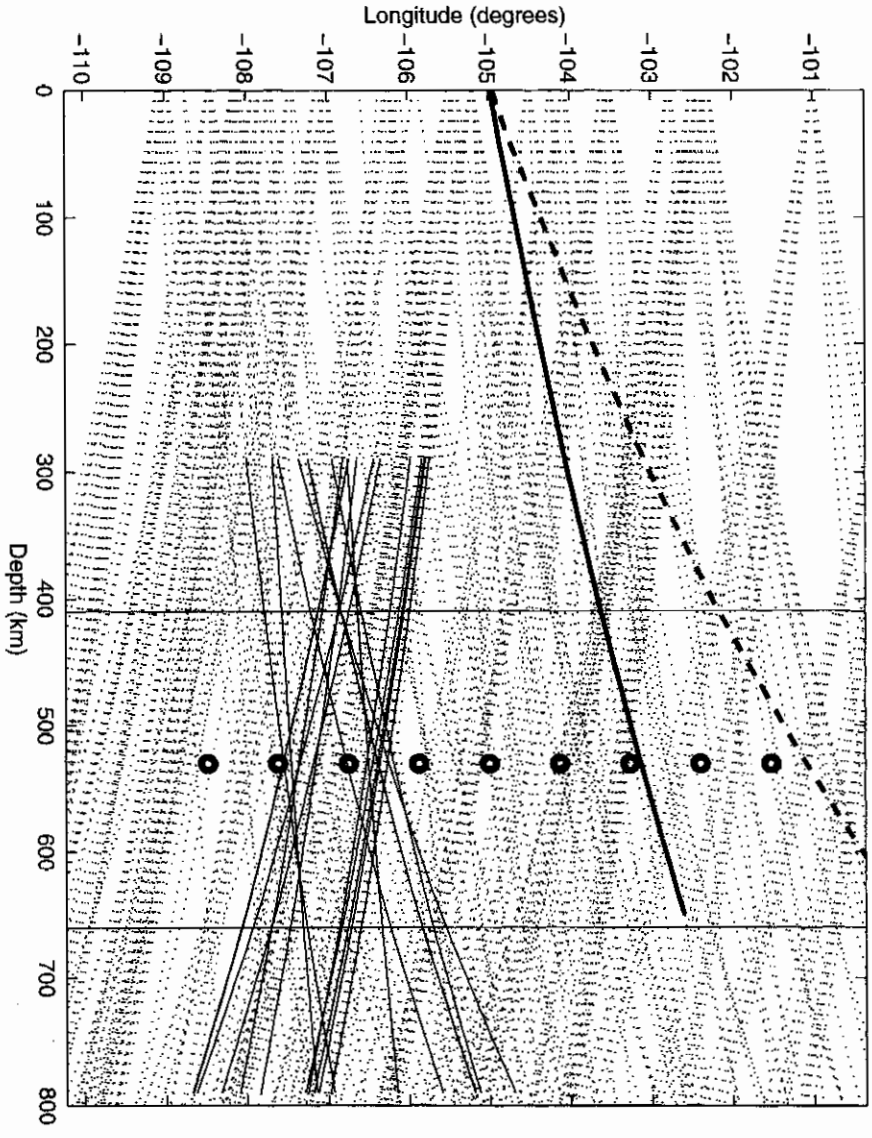

Figure 2. East-west projection of P_dS ray paths in upper mantle. All 365 P_dS ray paths used from the Rocky Mountain Front data set are shown as dotted lines. Circles at binning depth of 530 km depth indicate the 75 km spacing between bins (50% spatial overlap between bins). Rays sampling a representative bin are shown as thin solid lines. The direct P and $P_{660}S$ ray paths for a typical event are shown as the thick dashed and thick solid lines, respectively.

Thus, our absolute depths are dependent upon our assumed V_P and V_S models. The P_dS move-out is defined as

$$\delta T_{P_dS}(p) = T_{P_dS}(p) - T_{P_dS}(0) \tag{3}$$

Small variations (5% or less) in the velocity model produce less than 1 s of variations in the predicted moveout.

2.4. Lateral Heterogeneity Corrections

Another source of P_dS timing variations is lateral P and S wave velocity heterogeneity. The magnitude of a typical P_dS time shift due to lateral heterogeneity can be estimated using

$$\Delta T_{P_dS} = \Delta T_S - \frac{P_{len}}{S_{len}} \Delta T_S \frac{\delta t_P}{\delta t_S} \approx 0.5 \Delta T_S \approx \Delta T_p \tag{4}$$

where ΔT_S and ΔT_P are the observed S and P wave relative travel time residuals, P_{len}/S_{len} is the ratio of P to converted S wave path lengths in the region of interest, and $\delta t_S / \delta t_P$ is the slope of a linear fit to observed P versus S wave travel time residuals. The ratio of path lengths for $P_{410}S$ is 1.14 at a ray parameter of 0.06 s/km, and we find a $\delta t_S / \delta t_P$ of 2.4 from a bi-variate regression of P and S wave travel time residuals from the Rocky Mountain Front experiment (Figure 3). Thus, a typical P_dS lateral heterogeneity timing correction is approximately equal to a teleseismic P residual or about one-half a teleseismic S residual (Figure 4). Given the maximum 6 s range of teleseismic S residuals and 3 s range of teleseismic P residuals observed beneath the RMF array, we expect the range of P_dS timing corrections to be approximately 3 s.

In practice, we determine P_dS travel time delays due to lateral heterogeneity by directly integrating through local P and S wave tomographic models:

$$\Delta T_{P_dS} \int_{S-ray} \frac{dl}{\delta V_S(x)} - \int_{P-ray} \frac{dl}{\delta V_P(x)} \tag{5}$$

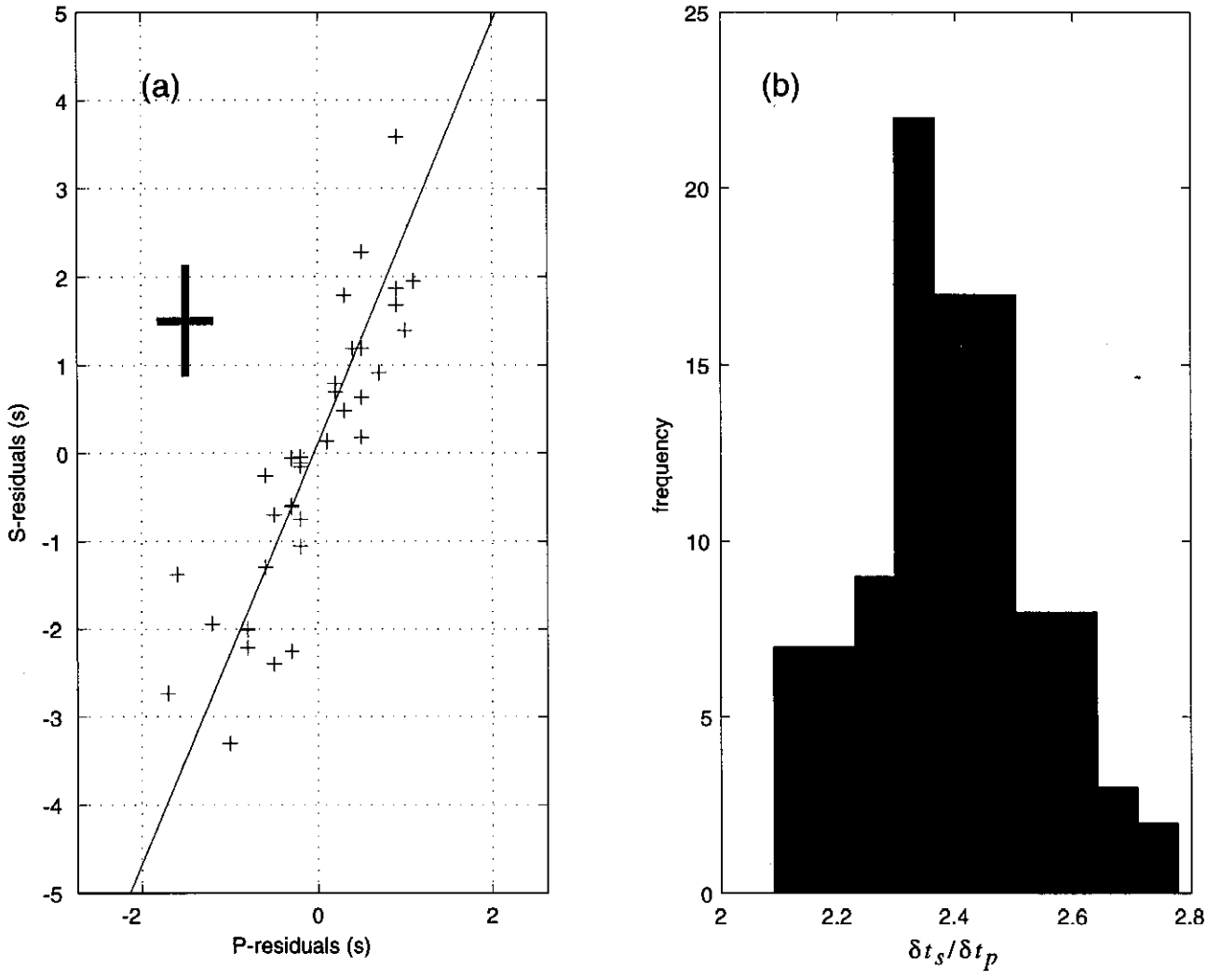

Figure 3. (a) Coincident (same source and station) *P* [*Hessler and Humphreys*, 1996] and *S* [*Lee and Grand*, 1996] teleseismic travel time residuals from the Rocky Mountain Front Experiment. Best fitting slope $\delta t_p/\delta t_s$ = 2.4 determined using bi-variate regression [*Tarantola*, 1987]. Large cross in upper left-hand corner of plot indicates assumed standard deviation of *P* (0.2 s) and *S* (0.6 s) residuals. (b) Histogram of $\delta t_p/\delta t_s$ slope found via bootstrap resampling: Data are resampled and bi-variate regression applied. The mean and standard error of the histogram are 2.4 ± 0.3.

where *S* ray is the converted *S* ray path and *P* ray is the direct *P* ray path. Here, δV_S comes directly from the shear wave velocity model of *Lee and Grand* [1996] (Figure 5), integrated from the surface to 400 km depth. The δV_P values are estimated by rescaling the *S* model with $\partial lnV_S/\partial lnV_P$ = 1.3. This value is derived from the relation $\delta t_S/\delta t_P = (V_P/V_S)\,\partial lnV_S/\partial lnV_P$ [*Hales and Doyle*, 1967] using the observed $\delta t_S/\delta t_P$ of 2.4 and assumed V_P/V_S value of 1.84 [*Kennett and Engdahl*, 1991]. A histogram of the 365 calculated P_dS timing corrections is shown along with observed *P* and *S* wave travel time residuals in Figure 4, and a map view of P_dS corrections is shown in Figure 5. The distribution of the P_dS residuals is similar to the teleseismic *P* wave travel time residual distribution, as predicted by (4).

The lateral heterogeneity timing corrections are removed from the receiver functions by splitting the traces and applying the time shifts at 20 s (equivalent to 180 km depth). This trace splitting is done because applying the *S* wave time corrections at 0 s would cause incoherent stacking of the direct *P* wave arrival, Moho arrival, and its reverberations. We assume that the majority of the travel time heterogeneity results from structure shallower than 410 km, consistent with tomographic images produced from the RMF array [*Lee and Grand*, 1996; *Hessler and Humphreys*, 1996].

2.5. Error Estimation

Bootstrap resampling with replacement is performed in order to estimate the best stack trace and its error [*Efron and Tibshirani*, 1986]. One hundred realizations of each stack are calculated, and the mean and standard deviation of the stack are found from the resulting distributions. We bootstrap the depth of the discontinuities by picking the depth of the largest peak around the depths of 660 km (660 ± 50) and 410 km (410 ± 50) for every realization of each stack. This provides distributions of the depth of the $P_{660}S$ and $P_{410}S$ arrivals which are used to provide our best estimates of the discontinuity depth and standard error.

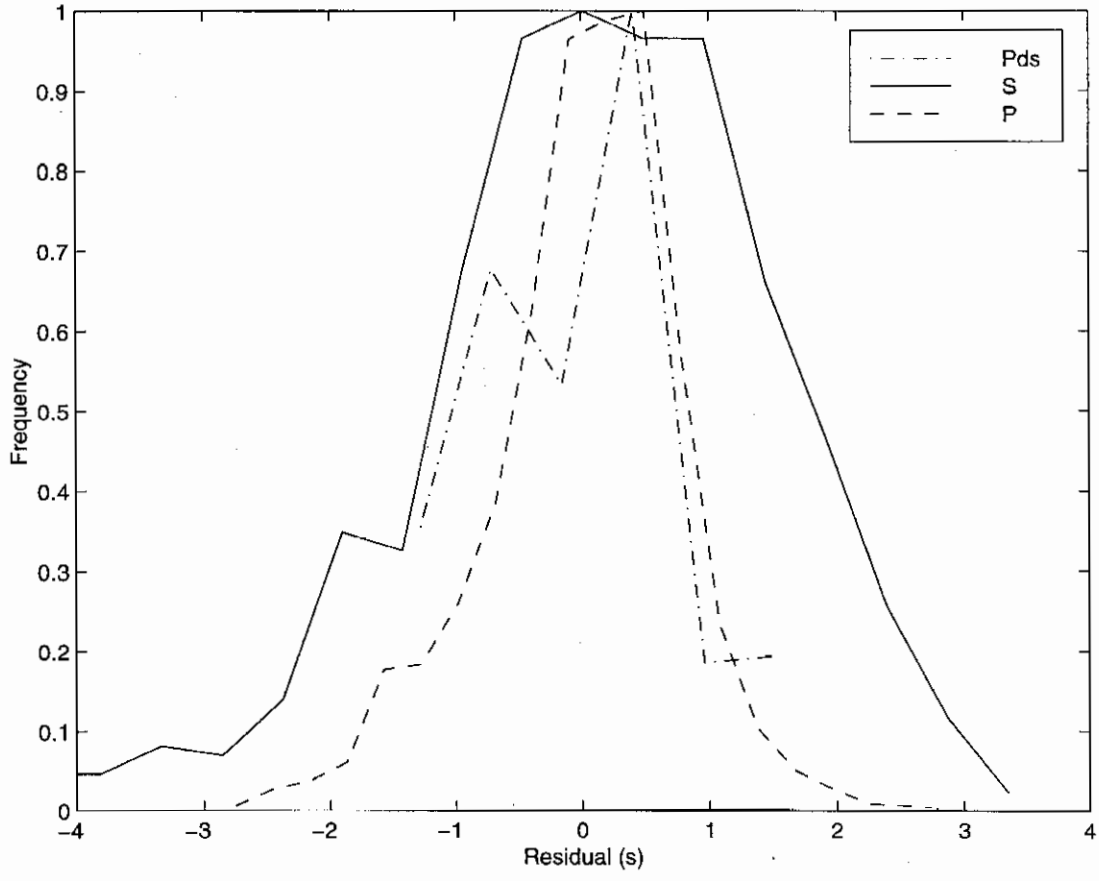

Figure 4. Normalized distribution of observed and predicted RMF travel time residuals. Dashed line denotes observed teleseismic *P* residuals [*Hessler and Humphreys*, 1996]; solid line denotes observed teleseismic *S* residuals [*Lee and Grand*, 1996]; dash-dot denotes P_dS timing corrections calculated by ray tracing through *Lee and Grand* [1996] tomographic model (equation (5)).

2.6. Summary of Stack Processing

From all observed teleseismic *P* wave arrivals, 365 radial receiver functions are computed. The radial receiver functions are binned based on a 530-km depth piercing point. Lateral velocity heterogeneity timing corrections are determined and applied to each trace. Traces are aligned by increasing ray parameter and stacked along move-out curves constructed from the velocity model TNA with V_P/V_S ratio of 1.84. The mapping of time to depth is performed at the time of stacking along the predicted moveout curves. The best stack trace and its error for each bin are estimated using the bootstrap resampling technique.

3. Results

3.1. Global Stack

To assess the average discontinuity structure beneath Colorado, phasing analysis of the entire data set is performed. Phasing analysis is performed by stacking the data along trial P_dS move-out curves for a range of discontinuity depths. If an arrival is truly a P_dS arrival (as opposed to reverberation or noise), then the amplitude of the arrival should be maximized when the correct move-out curve (i.e., phasing depth) is used. The phasing diagram (Figure 6) shows that *Pds* arrivals phase properly at nominal depths of 410 and 660 km. Candidate discontinuities near 300 and 520 km do not phase well. This may be due to the small amplitude of the 520 km discontinuity and possible contributions from shallower reverberations for the 300 km discontinuity. Unmodeled three-dimensional velocity structure may also contribute to the offset of peak amplitudes from the diagonal line.

A P_dS move-out corrected stack of the entire Rocky Mountain Front data set is shown in Figure 7. The transition zone arrivals are found at 419 and 677 km depths, resulting in a transition zone thickness of 258 km. A weak arrival at 520 km depth is also observed. Stacks were also performed by summing data along the reverberatory Pp_dS curves in order to test whether the observed arrivals might be reverberations from shallower discontinuities. These tests show that only the arrivals at 160 and 205 km stack with greater amplitudes along the reverberation curves.

3.2. Mantle Discontinuity Image

In order to examine lateral variations in mantle discontinuity structure, stack traces are made from all receiver functions with

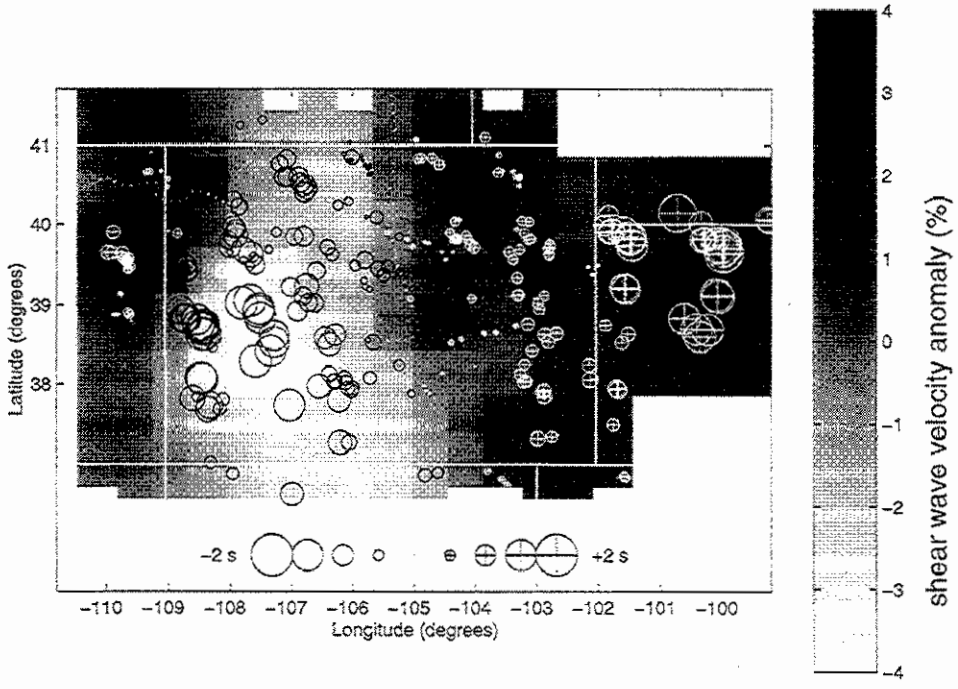

Figure 5. Shear wave velocity structure at 100 km depth [*Lee and Grand*, 1996] and $P_d s$ timing corrections in seconds. The circles are the $P_d s$ lateral heterogeneity timing corrections and range from ± 1.5 s.

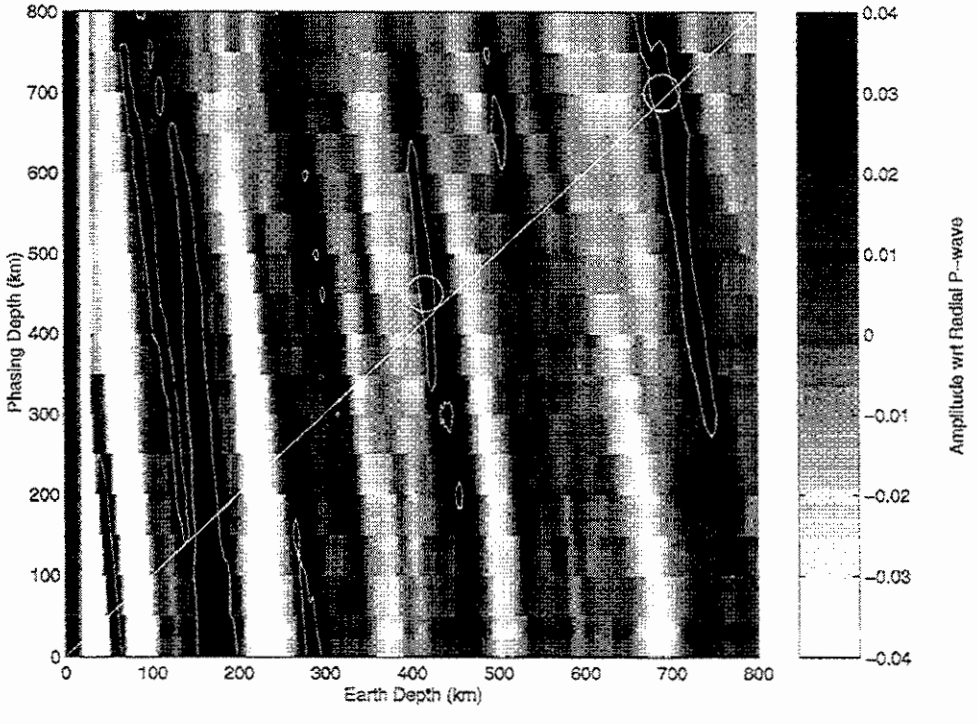

Figure 6. Discontinuity phasing diagram for all radial receiver functions. Phasing diagram is constructed by stacking all receiver functions using the move-out appropriate for a given "phasing depth", plotting the resulting stacked receiver function in grey scale, and then repeating the process for the next phasing depth. A peak in the phasing depth diagram at Earth depth equal to phasing depth (diagonal line) should appear for true $P_d s$ conversions. The +3.5% amplitude level is contoured. Maximum amplitudes of the 410 and 660 km arrivals are given by circles. The strong arrivals above 220 km depth are crustal arrivals.

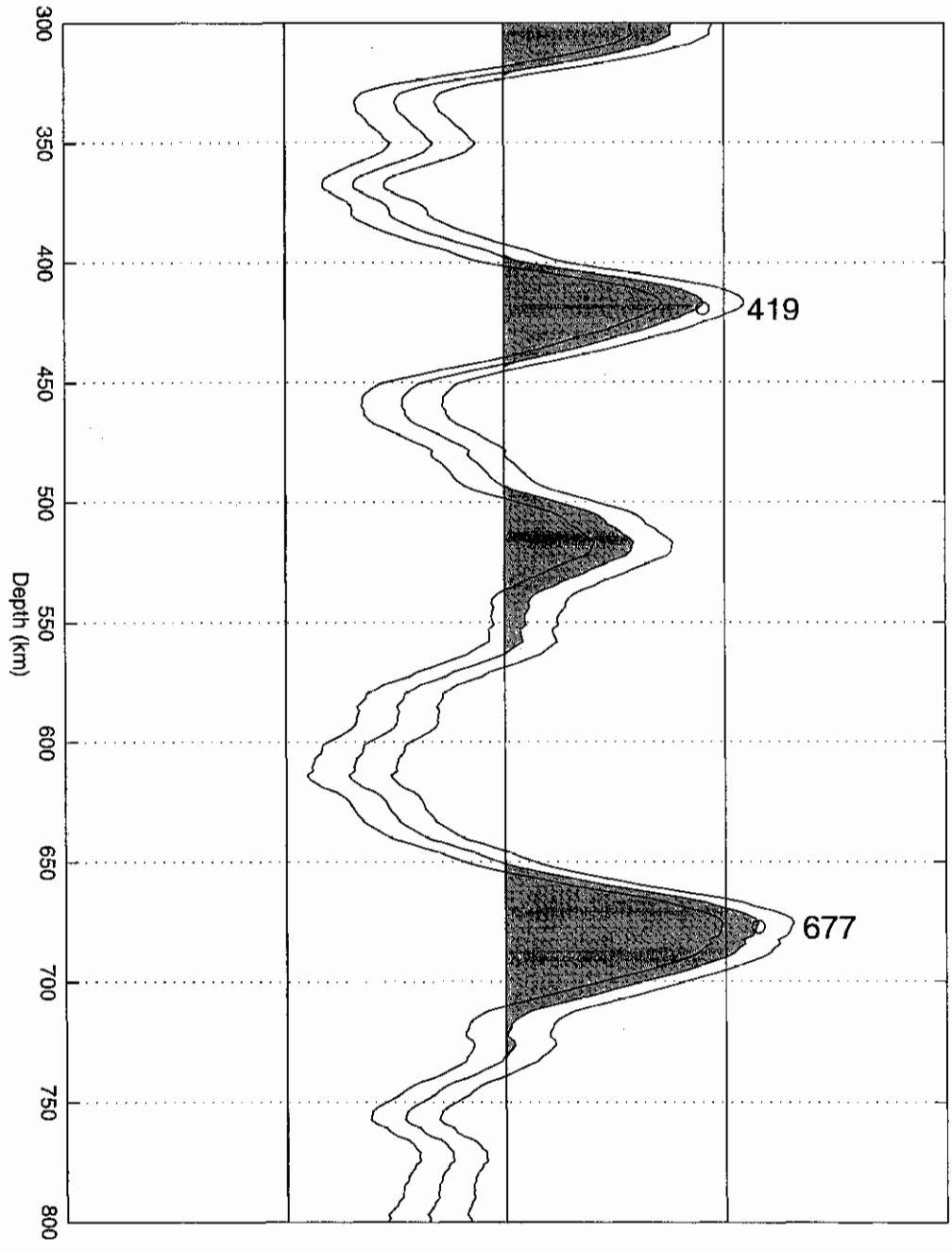

Figure 7. Move-out corrected stack of all radial receiver functions. The middle trace is the mean stack, and the thin lines represent 95% confidence limits calculated using a bootstrap resampling algorithm, with center line representing mean stack value (positive portion shaded). The vertical lines are ±10% of radial P wave amplitude. Significant positive amplitude $P_d s$ arrivals are observed from the 410 and 660 km discontinuities, peaking at 419 and 677 km depth.

530 km $P_d s$ piercing points within 150 km square geographical bins. Adjacent bins overlap by 50%, and each bin is required to have a minimum of 20 traces. Stack traces plotted together produce a spatial image of mantle discontinuity structure. Cross sections through the image (Figure 8) show the same major arrivals seen in the global stack: clear 410 and 660 km discontinuities and an intermittent 520 km discontinuity. In east-west cross sections, A-A' through E-E', a depression of the 410 km discontinuity by 10 km from the Rocky Mountains to the Colorado High Plains is observed while the 660 km discontinuity remains relatively flat. The 660 km discontinuity is more complex in the southern part of the study area (D-D' through F-F') than in the northern part (A-A' through C-C'). In the north-south cross sections (G-G' through O-O'), variations in the dip and average depth of the 410 km discontinuity are observed. At the southern end of cross sections (G-G' through K-K'), the 660 km discontinuity is observed at a depth of around 700 km. This is consistent with its depression in the E-W cross sections. The 520

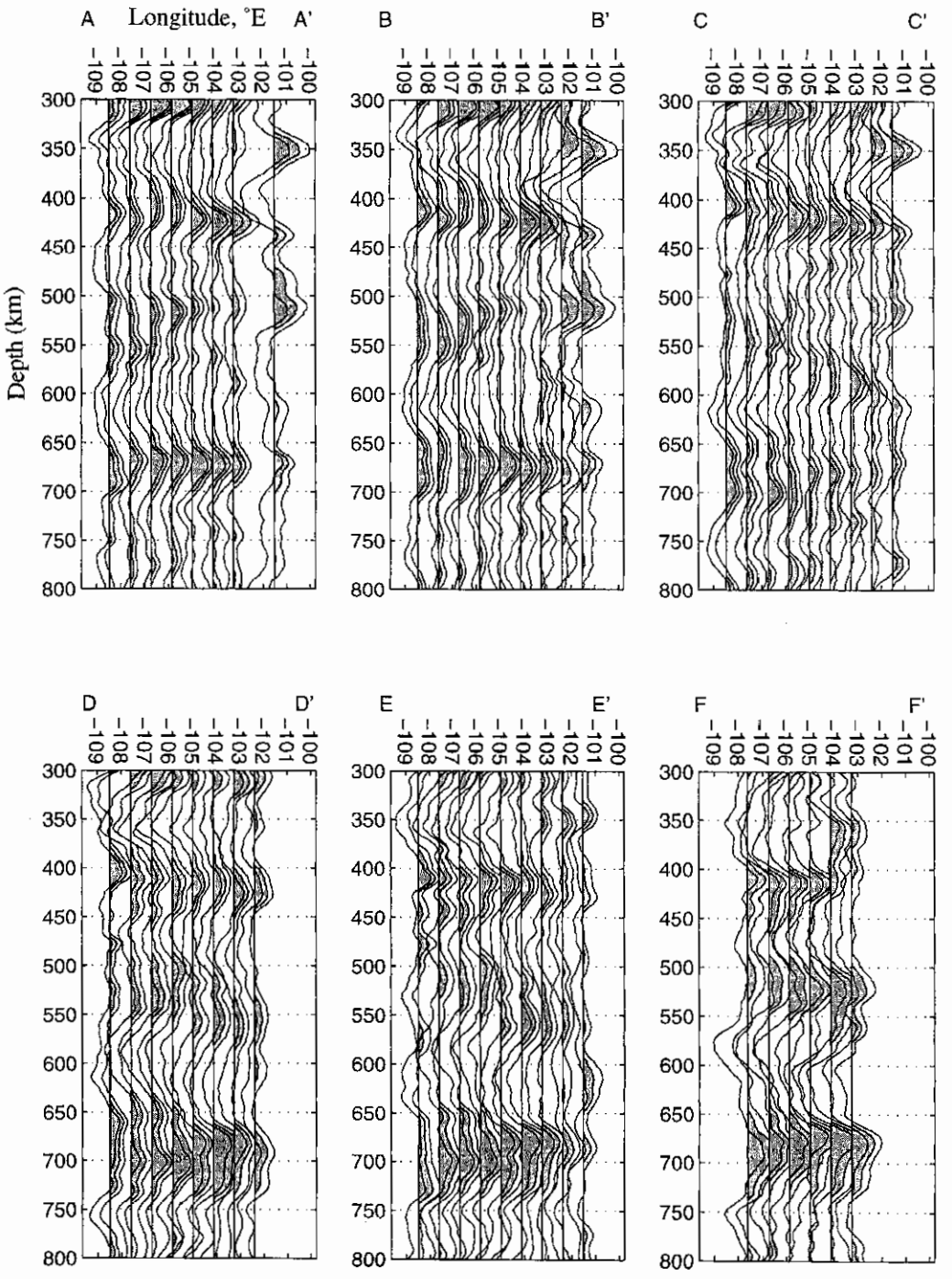

Figure 8. Mantle discontinuity image using 150 km square bins. Cross-section labels at the top of each graph as in Figure 1. Positive amplitude arrivals are shaded, and the spacing between traces is 10% of the radial *P* wave. For east-west cross sections (A-A' through F-F'), longitude in degrees is plotted at the top; for north-south cross sections (G-G' through O-O'), latitude in degrees is plotted at the top. Vertical axis on all plots is depth in kilometers.

km discontinuity is most coherent in cross section I-I', but in general is not prominent.

Many of the 660 and 410 km arrivals lack well-defined peaks, making assessment of the depth of these discontinuities difficult. To further quantify discontinuity topography, the depth of the maximum amplitude between 360 - 460 km and 610 - 710 km is picked from each realization of the bootstrap stack. The resulting distributions are used to estimate the average depth to the 410 and 660 km discontinuity for each bin (Figure 9). To mitigate the effects of noise, only arrivals with peak amplitudes greater than 3% of the radial *P* wave are used in the histograms. The shape of the distribution gives an indication of the quality of the depth estimate, with narrow-peaked histograms indicating the most tightly constrained depth estimates. Estimates of the discontinuity depths are found using a trimmed median so that secondary peaks in the distributions do not bias the depth estimates. The

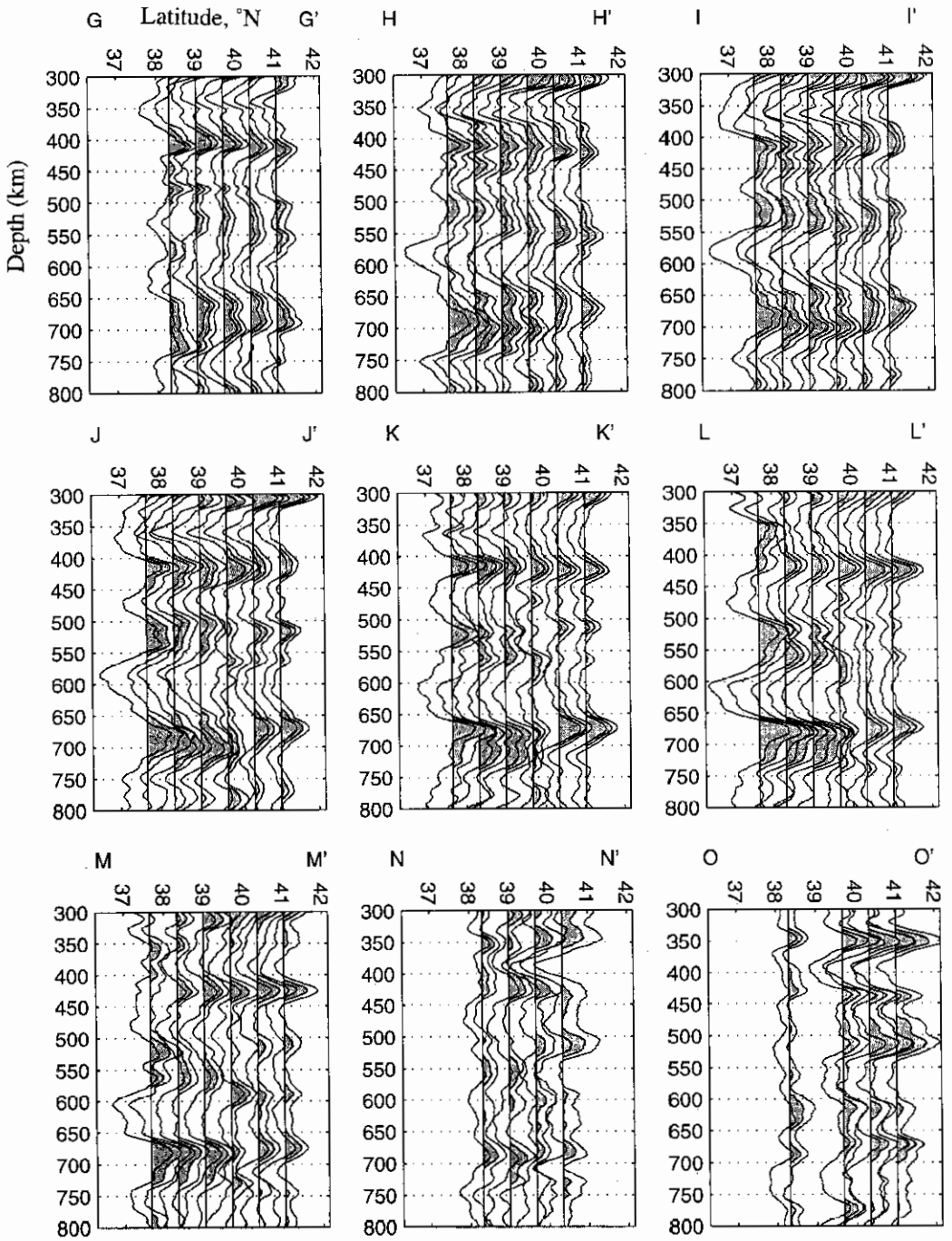

Figure 8. (continued)

discontinuity depth is estimated from the median of measurements within ± 20 km of the mode of the distribution. A histogram of these depth estimates (Figure 10) reveals that the magnitude of the 660 topography (30 km) is significantly larger than the magnitude of the 410 topography (20 km). This finding is insensitive to the effects of velocity heterogeneity above 410 km, which would affect the discontinuities equally.

Using the depths derived from the histograms in Figure 9, the correlation between the 410 and 660 km discontinuity topography is investigated in Figure 11. The 660 km discontinuity is found to deepen in western Colorado (western side of cross sections C-C', D-D', and E-E') with no significant variation in the 410 km discontinuity. This lack of correlated discontinuity topography suggests that lateral heterogeneity has been properly accounted for. Transition zone thickness is determined by subtracting the depth of the 660 km discontinuity from that of the 410 km discontinuity for each bin. The resulting map of transition zone thickness variations (Figure 12) shows a thick transition zone beneath western Colorado and a thin transition zone beneath the Colorado High Plains and northernmost Colorado.

3.3. Effect of Travel Time Corrections

In order to further assess the effect of lateral heterogeneity corrections, we compare images made both without (Figure 13a)

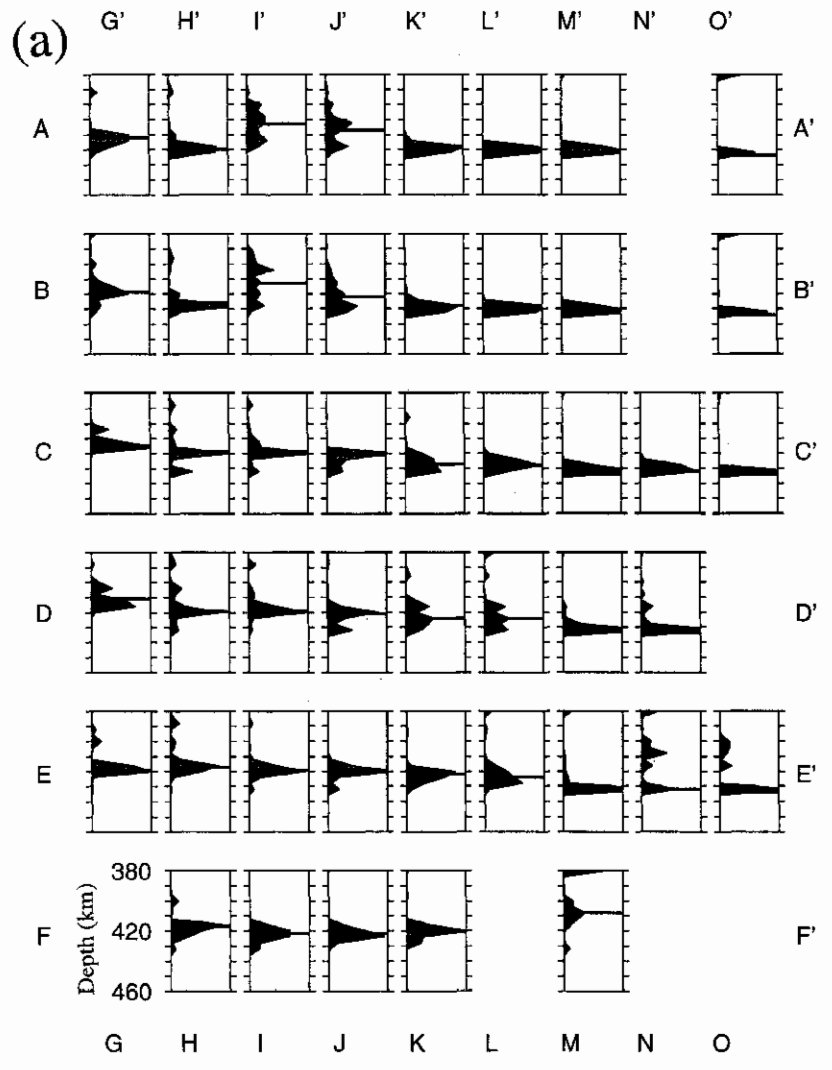

Figure 9. Histograms of (a) 410 and (b) 420 km discontinuity depths. The depth of the peak amplitude at 420 ± 40 and 690 ± 40 km depth is calculated using bootstrap resampling for each bin. Bins are arranged in geographic order with cross-sectional labels as in Figure 1. Vertical axis on each plot is depth in kilometers (scale on lower left bin), and horizontal axis is histogram frequency. The horizontal lines show the trimmed median of each distribution. The majority of the distributions are bell-shaped with standard errors less than 5 km.

and with (Figure 13b) travel time corrections. To assess the global nature of the timing correction on the image, we have plotted all 54 bins used in the study. The most obvious difference between the two images is that the timing corrections depress both the 410 and 660 km discontinuities toward the eastern half of the array. This is consistent with correction for the fast upper mantle observed in this region (Figure 5). The image coherence is not changed significantly because the 0-3 s timing corrections are small with respect to the 10 s period of the traces. Since our lateral velocity heterogeneity corrections are limited to models from 0 to 400 km depth, corrections for possible lateral heterogeneity within the transition zone itself have not been made. A recent model by *Van der Lee and Nolet* [1997] shows a high-velocity anomaly within the transition zone beneath southwest Colorado. Accounting for this particular transition zone velocity heterogeneity will only increase the thickness of the transition zone in this region.

3.4. Randomized Midpoint Image

To test the hypothesis that the discontinuity structure beneath the Rocky Mountain Front array is continuous and relatively flat (i.e., less than 10 km of discontinuity topography), we present an image in which all of the midpoints of the $P_d s$ rays are randomized (Figure 14) and then processed in exactly the same way as in the true stacks. This procedure maintains the coherence imposed by the spatial overlap and sharing of seismograms between adjacent bins. The same statistical resolution is maintained by keeping the number of traces per bin the same as in the true images. Lateral heterogeneity corrections are applied to the traces prior to midpoint randomization. If all of the discontinuity structure was continuous and flat, then the lateral coherence of this image should be similar to the coherence of Figure 13b. A comparison of the correct (Figure 13b) and

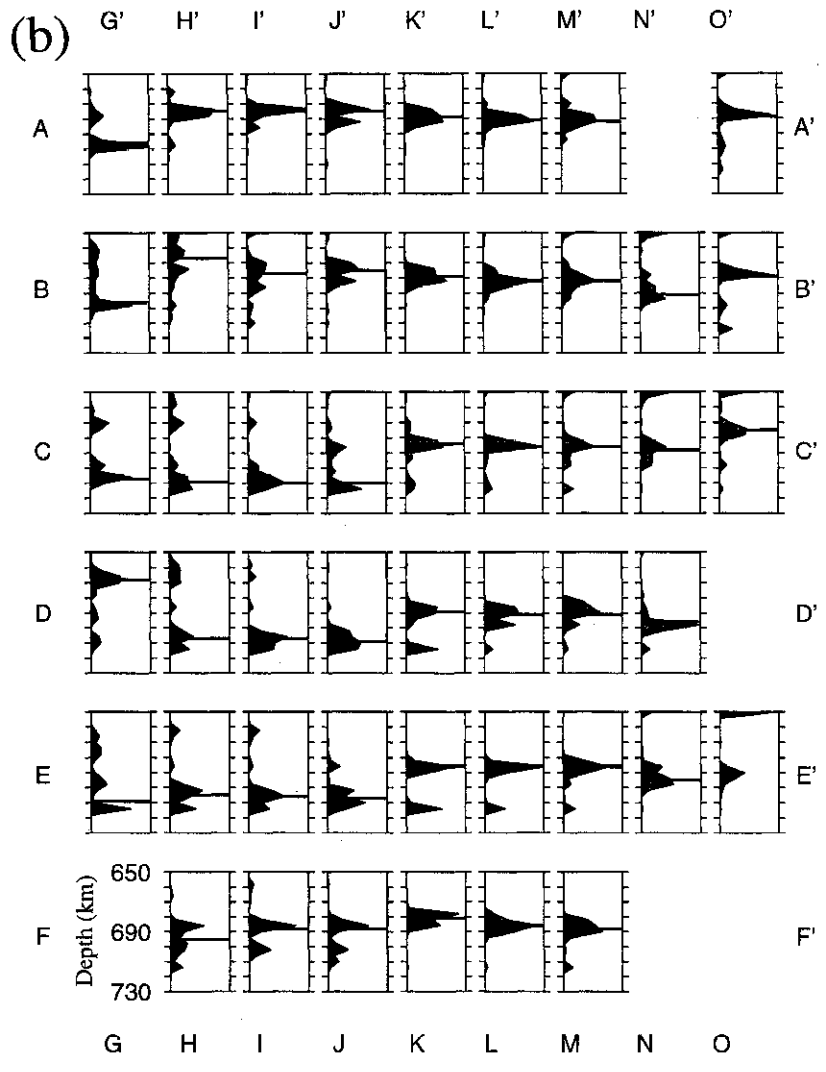

Figure 9. (continued)

randomized (Figure 14) midpoint images shows a significant difference in lateral coherence. We suggest that the P_dS timing variations due to true discontinuity topography contribute to stack incoherence in the randomized stacks.

3.5. Effect of Crust and Sediments

Midpoint stacking focused on isolating the $P_{moho}S$ arrival shows that the Moho timing beneath the RMF array ranges from 4.9 to 6.8 s [*Keller et al.*, 1996]. Corresponding P_dS timing variations associated with these Moho variations are ± 0.3 s [*Bostock*, 1996], minor with respect to the 3-4 s variations in $P_{410}S$ and $P_{660}S$ observed. The presence of thick sedimentary basins can produce reverberations and mode conversions [e.g., *Levander and Hill*, 1985] which can degrade the receiver function deconvolution, but has a negligible effect in the frequency band we are working in (10 -30 s).

4. Discussion

Our primary findings regarding the mantle discontinuity structure beneath Colorado are as follows:

1. Up to 40 km of transition zone thickness variation is observed.
2. More 660 km discontinuity topography (30 km) is observed than 410 km discontinuity topography (20 km).
3. In southwest Colorado, the 660 km discontinuity deepens by 20 km, approximately coincident with high velocities imaged in the lower transition zone by *Van der Lee and Nolet* [1997].
4. The 410 km discontinuity deepens by 10 km beneath the Colorado High Plains, while the 660 km discontinuity remains relatively flat.
5. An intermittent 520 km arrival is observed with about half the amplitude of the $P_{660}S$ arrival.

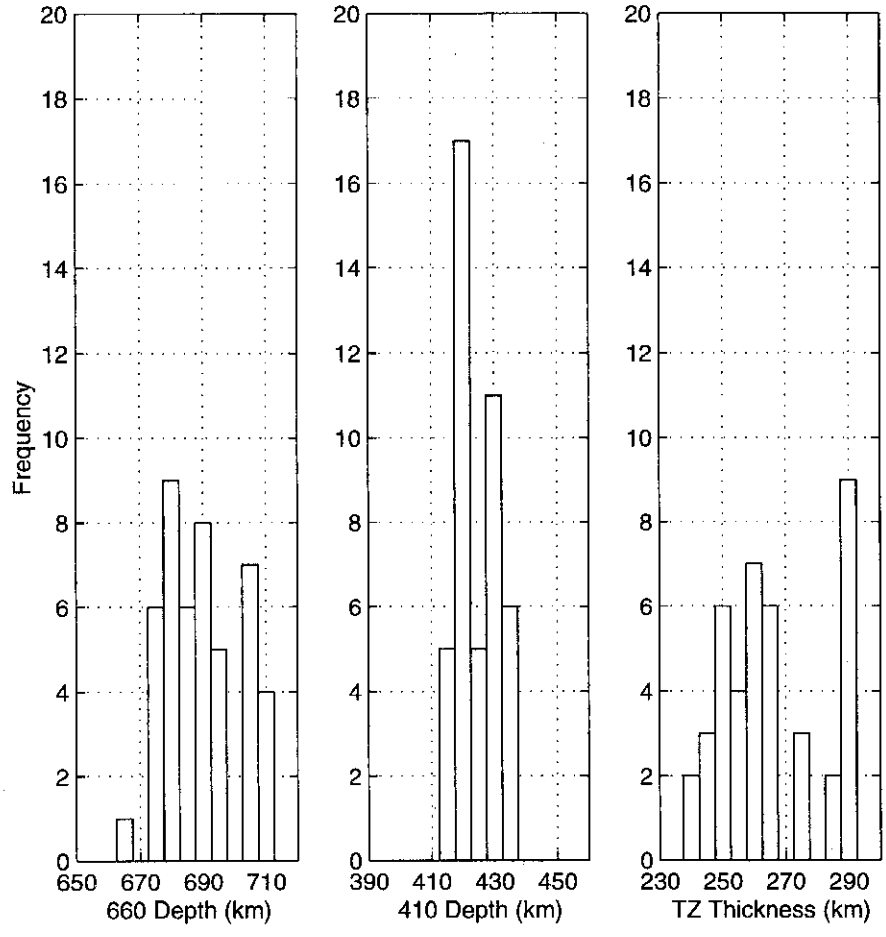

Figure 10. Distribution of 410 and 660 depth and transition zone thickness for entire array, determined from results shown in Figure 9.

The lack of a strong correlation between 410 and 660 km discontinuity topography suggests that the discontinuity topography beneath the southern Rockies cannot be fully explained by the simplest hypothesis regarding its origin. This hypothesis (the vertical coherent thermal model) assumes that the 410 and 660 km discontinuities are purely described as the $\alpha \rightarrow \beta$ olivine and γ-olivine $\rightarrow$ magnesiowustite + perovskite phase transformations whose topography is modulated by vertically coherent thermal anomalies in the transition zone [e.g., *Bina and Helffrich*, 1994]. The fundamental diagnostic of this model is that it predicts an anticorrelated movement of the 410 and 660 due to the different signs of the respective Clapeyron slopes. As shown in Figure 11, the discontinuity topography is not strongly correlated either positively or negatively. This noncorrelated discontinuity topography suggests that any thermal anomaly creating topography at one boundary is not necessarily present at the other. At these short scale lengths (150 - 600 km) other mechanisms can create discontinuity topography. Other mechanisms which have been suggested include phase transformations of the garnet-pyroxene system [*Anderson*, 1989], chemical layering [*Anderson*, 1989], variations in mantle hydration [*Wood*, 1995], and kinetic effects [*Solomatov and Stevenson*, 1994].

The 10 km depression of the 410 km discontinuity beneath the Colorado High Plains cannot be simply explained. If we assume a thermal origin for this topography and a Clapeyron slope of 3 Mpa/°C [*Bina and Helffrich*, 1994], this offset requires the mantle at 410 km to be 100°C warmer beneath the High Plains than beneath the Rocky Mountains. At shallower (< 200 km) depths, the tomographic models of *Lee and Grand* [1996] and *Hessler and Humphreys* [1996] indicate slower velocity beneath the Rockies than beneath the High Plains. However, the velocity model of *Van der Lee and Nolet* [1997] shows relatively low velocity mantle beneath the High Plains at transition zone depths. Therefore either the upper mantle thermal structure is not vertically coherent in this region, or something other than thermal processes is perturbing the velocity and discontinuity structure.

Our finding of 40 km of transition zone thickness variations beneath Colorado may seem surprising given previous $P_d s$ studies which suggest less than 20 km of transition zone thickness variations [*Stammler et al.*, 1992; *Vinnik et al.*, 1996; *Bostock*, 1996]. However, *Gurrola* [1995] found 20 km of topography on the 410 and 660 km discontinuities over short (less than 300 km) wavelengths using $P_d s$ phases at station ANMO, just 500 km south of our study area. Hypotheses for explaining the large amount of discontinuity topography that we observe are considered below.

We discount the hypothesis that the topography observed is due to inadequate lateral heterogeneity corrections or noise. We instead suggest the lack of positively correlated discontinuity

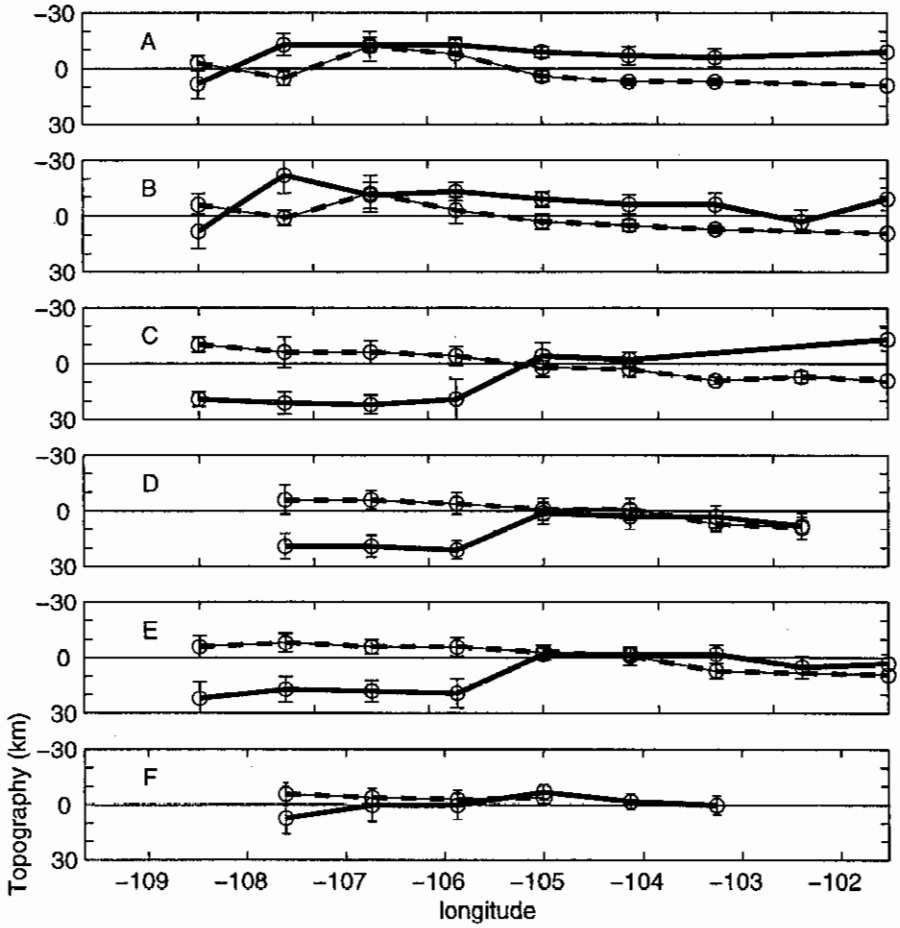

Figure 11. East-west cross sections of discontinuity topography. The 660 km discontinuity is given by solid line; 410 km discontinuity is given by dashed line. Discontinuity depths are from Figure 9; error bars represent standard deviation. The mean depth of the discontinuities has been removed for this plot. Cross-sectional labels as in Figure 1. Note the lack of correlated or anticorrelated discontinuity behavior.

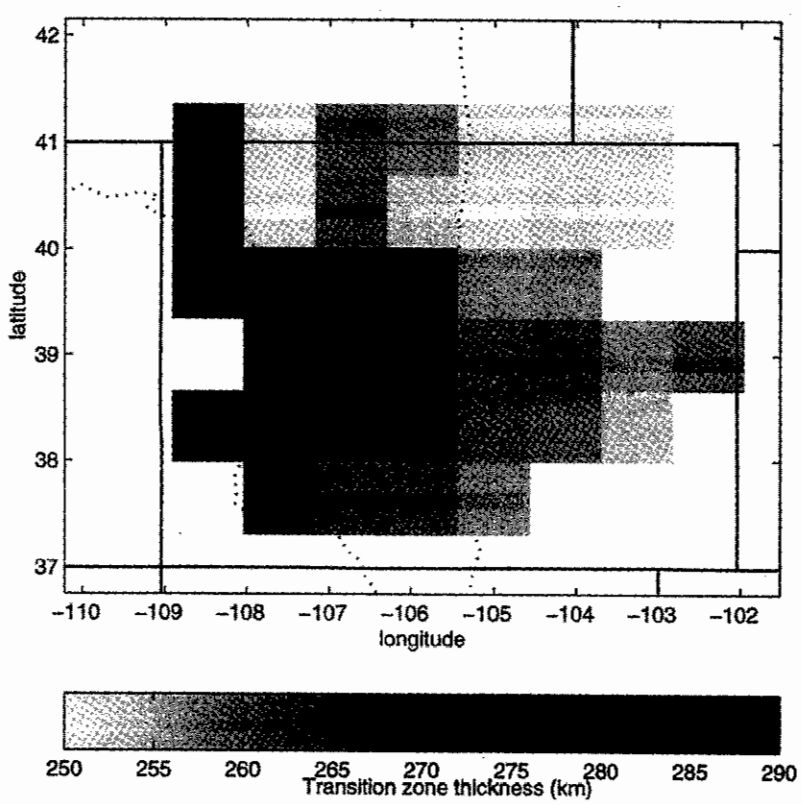

Figure 12. Transition zone thickness variations found by subtracting 410 km discontinuity depth from 660 km discontinuity depth for each bin. Darker shading denotes greater transition zone thickness.

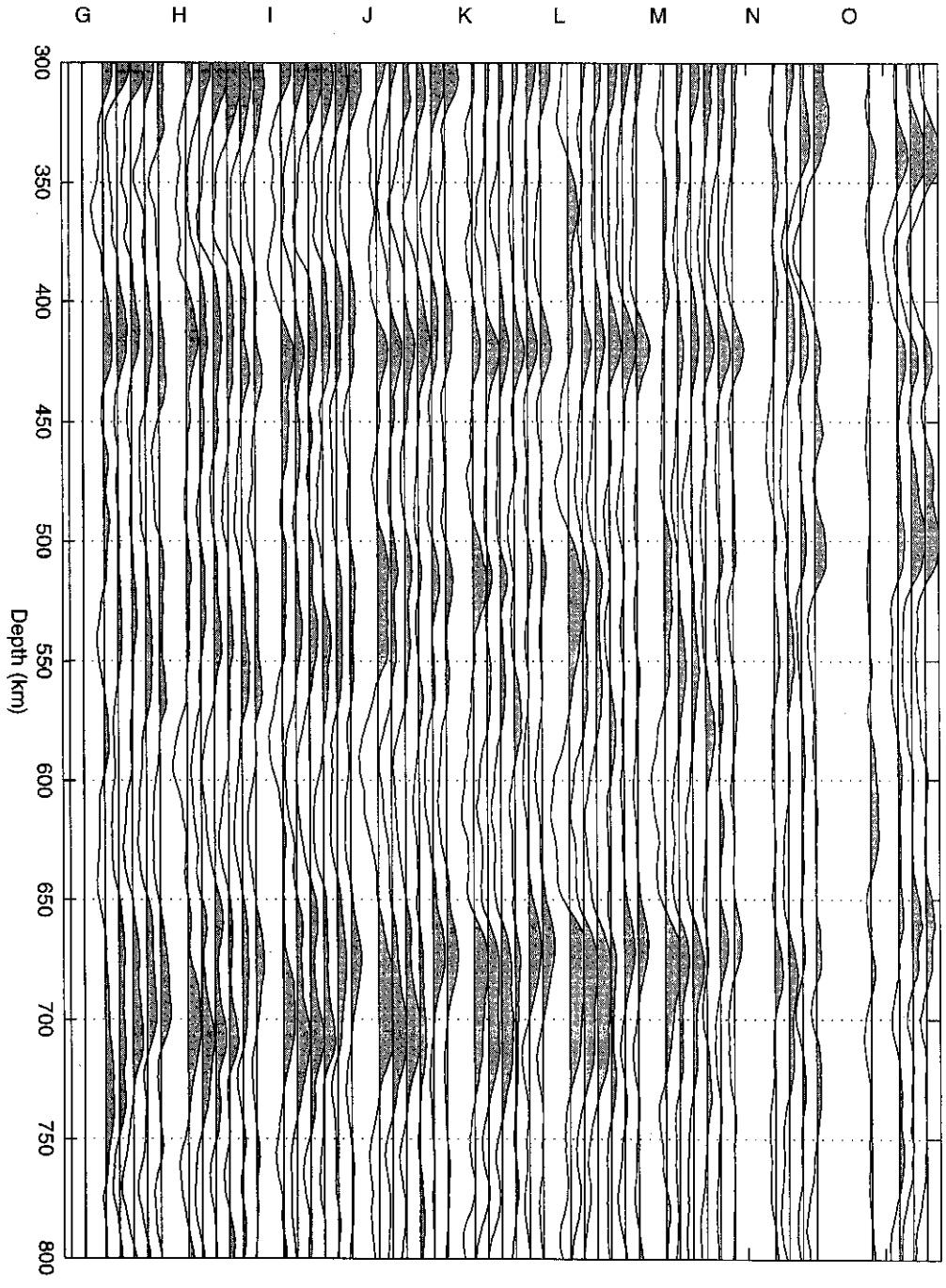

Figure 13. Test of lateral heterogeneity corrections: (a) stacks without timing corrections; (b) stacks with timing corrections. All bins are shown starting with cross section G-G' at the west end of the array and finishing with cross section O-O' at the east end of the study area. Spacing between traces is 10% of the radial *P* wave.

topography, and the comparison of predicted versus calculated P_dS timing variations is evidence against significant biasing of our discontinuity topography by inadequate lateral heterogeneity corrections. The loss of coherence in the randomized midpoint images (Figure 14) also suggests that the spatially coherent topography imaged in Figure 8 is required by the data.

Another potential explanation for our results is that Colorado possesses a uniquely heterogeneous transition zone. Certainly, the presence of a slab in the transition zone beneath southwest Colorado [*Van der Lee and Nolet*, 1997] would increase the amount of transition zone topography. Similar processing of array data from the 1993 Snake River Plain array has shown equally large variations in transition zone structure [*Dueker and Sheehan*, 1997]. However, given that our studies are the first to achieve such high density spatial images of discontinuity structure by common depth point stacking of broadband array data, we believe that it would be premature to state that Colorado possesses a uniquely heterogeneous transition zone.

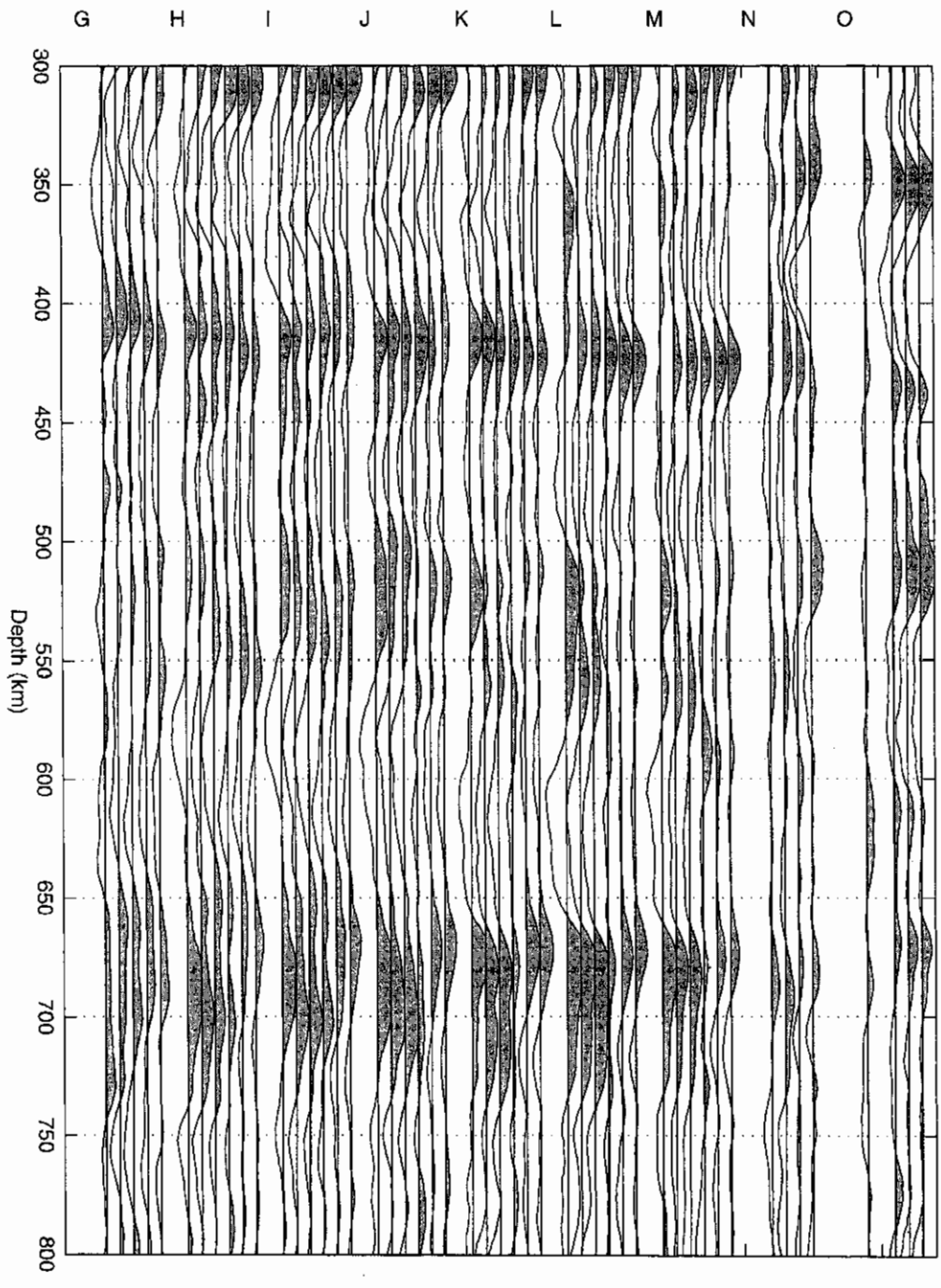

Figure 13. (continued)

Our favored explanation for finding large discontinuity topography over such a short spacial scale is that our dense array of stations and subsequent processing provide improved spatial resolution than in previous P_dS studies. Single-station stacks to isolate $P_{660}s$ and $P_{410}s$ energy are typically performed over a range of back azimuths and incidence angles. Thus these stacks spatially average any 410 and 660 km topography within an annulus between 140 and 230 km and between 280 and 450 km in diameter, respectively (see Figure 2). Further support for short scale length transition zone discontinuity structure is provided by studies of the origin of the large-amplitude variations observed for discontinuity interaction phases. These studies suggest that 20-40 km undulations of the 660 and 410 km discontinuities over 200-400 km scale lengths will cause significant defocusing of the wave field consistent with the intermittent visibility of $P_{660}s$ arrivals [*Van der Lee et al.*, 1994] and $P_{410}P$ arrivals [*Neele and Snieder*, 1992].

We suggest that the relatively large-amplitude and short-wavelength topography observed on the 410 and 660 km discontinuities is not due exclusively to thermal heterogeneity. If this were the case, then temperature anomalies of the order of 250°C would be required [*Bina and Helffrich*, 1994]. The 410 and 660 km discontinuities are associated with 4-6% increases in density, thus topography on these boundaries would create

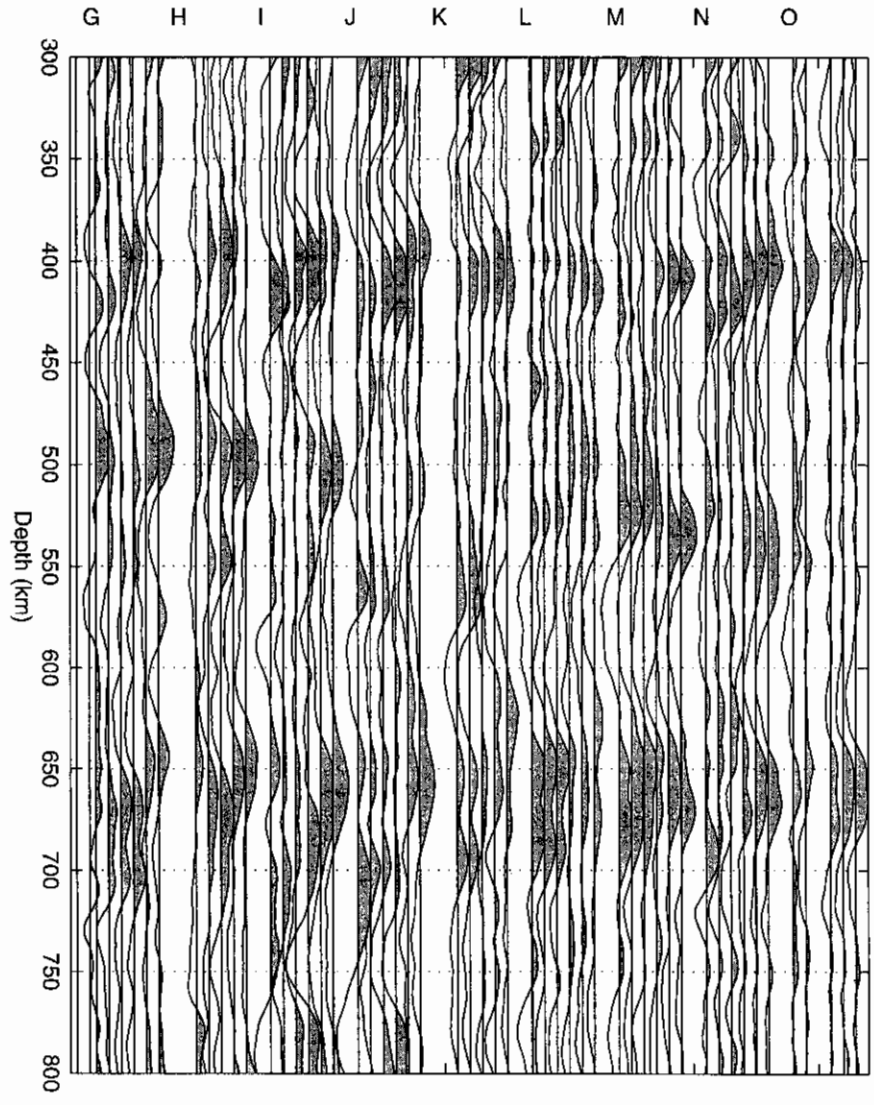

Figure 14. Randomized midpoint image (timing corrections applied before midpoint randomization). Compare spatial coherence with Figure 13b.

significant density anomalies. In the isostatic limit, 30 km of discontinuity topography could create kilometer scale free surface topography and meter scale geoid signal, depending upon mantle viscosity structure. Therefore, until modeling is performed, we hesitate to interpret the effect of the discontinuity topography on surface topography. The effects could be quite significant to the mantle flow patterns and hence the mechanism of uplift of the Colorado Rockies and High Plains [e.g., *Sheehan et al.*, 1995; *Gregory and Chase*, 1994].

5. Conclusions

Study of the mantle transition zone beneath Colorado reveals 20 km of topography on the 410 km discontinuity, 30 km of 660 km discontinuity topography, and 40 km of transition zone thickness variations. The 410 and 660 km topographies are not positively correlated, which suggests that upper mantle lateral velocity heterogeneity is not biasing our results. In southwestern Colorado, a complex 660 km discontinuity is observed, consistent with the presence of a slab extending through the transition zone [*Van der Lee and Nolet*, 1997]. We do not observe anticorrelated discontinuity topography, contrary to that predicted for phase transitions modulated by vertically coherent thermal anomalies. Results of a similar broadband array study of mantle discontinuity structure beneath the Snake River Plains [*Dueker and Sheehan*, 1997] also reveals significant topography on the 410 and 660 km discontinuities. Taken together, these two studies indicate that 200-500 km wavelength undulations in the western U.S. transition zone discontinuity structure might be a common occurrence. If so, then the thermal structure at the 660 and 410 km discontinuity beneath the western United States is complex, and/or other mechanisms such as chemical layering, hydration effects, or mineral reactions of the garnet-pyroxene system are creating significant discontinuity topography.

Acknowledgments. We thank Harold Gurrola and two anonymous reviewers for careful reviews which helped improve the paper. This research was supported by National Science Foundation grants EAR-9405542 and EAR-9319008.

References

Alsina, D., R. L. Woodward, and R. K. Snieder, Shear-wave velocity structure in North America from large-scale waveform inversions of surface waves, *J. Geophys. Res.*, *101*, 15,969-15,986, 1996.

Anderson, D. L., *Theory of the Earth*, Blackwell Sci., Cambridge, Mass., 1989.

Bina, C. R., and G. Helffrich, Phase transition Clapeyron slopes and transition zone seismic discontinuity topography, *J. Geophys. Res.*, *99*, 15,853-15,860, 1994.

Bostock, M. G., *Ps* conversions from the upper mantle transition zone beneath the Canadian landmass, *J. Geophys. Res.*, *101*, 8393-8402, 1996.

Cassidy, J. F., Numerical experiments in broadband receiver function analysis, *Bull. Seismol. Soc. Am.*, *82*, 1453-1474, 1992.

Clayton, R. W., and R. A. Wiggins, Source shape estimation and deconvolution of teleseismic body waves, *Geophys. J. R. Astron. Soc.*, *47*, 151-177, 1976.

Clouser, R. H., and C. A. Langston, Effect of sinusoidal interfaces on teleseismic *P*-wave receiver functions, *Geophys. J. Int.*, *123*, 541-558, 1995.

Dueker, K. G., and A. F. Sheehan, Mantle discontinuity structure from midpoint stacks of converted *P* to *S* waves across the Yellowstone hotspot track, *J. Geophys. Res.*, *102*, 8313-8327, 1997.

Efron, B., and R. Tibshirani, Bootstrap methods for standard errors, confidence intervals, and other measures of statistical accuracy, *Stat. Sci.*, *1*, 54-77, 1986.

Flanagan, M. P., and P. M. Shearer, Global mapping of topography on transition zone velocity discontinuities by stacking SS precursors, *J. Geophys. Res.*, in press, 1997.

Gossler, J., and R. Kind, Seismic evidence for very deep roots of continents, *Earth Planet. Sci. Lett.*, *138*, 1-13, 1996.

Grand, S. P., Mantle shear structure beneath the Americas and surrounding oceans, *J. Geophys. Res.*, *99*, 11,591-11,621, 1994.

Grand, S. P., and D. V. Helmberger, Upper mantle shear structure of North America, *Geophys. J. R. Astron. Soc.*, *76*, 399-438, 1984.

Gregory, K. M., and C. G. Chase, Tectonic and climatic significance of a late Eocene low-relief, high-level geomorphic surface, Colorado, *J. Geophys. Res.*, *99*, 20,140-20,160, 1994.

Gurrola, H., Investigation of the upper mantle transition zone through velocity spectrum stacking of receiver functions, Ph.D. thesis, 259 pp., Univ. of Calif., San Diego, La Jolla, 1995.

Gurrola, H., J. B. Minster, and T. Owens, The use of velocity spectrum for stacking receiver functions and imaging upper mantle discontinuities, *Geophys. J. Int.*, *117*, 427-440, 1994.

Hales, A. L., and H. A. Doyle, *P* and *S* travel times anomalies and their interpretation, *Geophys. J. R. Astron. Soc.*, *13*, 403-414, 1967.

Hessler, K. E., and E. D. Humphreys, *P*-wave tomography of Colorado's upper mantle, *Eos Trans. AGU*, *77*, Fall Meet. Suppl., F467, 1996.

Humphreys, E. D., and K. G. Dueker, Western U.S. upper mantle structure, *J. Geophys. Res.*, *99*, 9615-9634, 1994.

Keller, G. R., A. F. Sheehan, and K. G. Dueker, Evolution of the crust in the Rio Grande Rift - Southern Rocky Mountain Region, paper presented at Annual Meeting, Geol. Soc. Am., Denver, Colo., Oct. 1996.

Kennett, B. L. N., and E. R. Engdahl, Traveltimes for global earthquake location and phase identification, *Geophys. J. Int.*, *105*, 429-465, 1991.

Langston, C. A., Corvallis, Oregon, crustal and upper mantle receiver structure from teleseismic *P* and *S* waves, *Bull. Seismol. Soc. Am.*, *67*, 713-724, 1977.

Lee, D., and S. P. Grand, Upper mantle shear structure beneath the Colorado Rocky Mountains, *J. Geophys. Res.*, *101*, 22,233-22,244, 1996.

Levander, A. R., and N. R. Hill, *P-SV* resonances in irregular low-velocity surface layers, *Bull. Seismol. Soc. Am.*, *75*, 847-864, 1985.

Neele, F., and R. Snieder, Topography of the 400 km discontinuity from observations of long-period $P_{400}P$ phases, *Geophys. J. Int.*, *109*, 670-682, 1992.

Nolet, G., S. P. Grand, and B. L. N. Kennett, Seismic heterogeneity in the upper mantle, *J. Geophys. Res.*, *99*, 23,753-23,766, 1994.

Paulssen, H., Evidence for a sharp 670-km discontinuity as inferred from *P* to *S* converted waves, *J. Geophys. Res.*, *93*, 10,489-10,500, 1988.

Shearer, P. M., Constraints on upper mantle discontinuities from observations of long-period reflected and converted phases, *J. Geophys. Res.*, *96*, 18,147-18,182, 1991.

Sheehan, A. F., G. A. Abers, C. H. Jones, and A. L. Lerner-Lam, Crustal thickness variations across the Colorado Rocky Mountains from teleseismic receiver functions, *J. Geophys. Res.*, *100*, 20,391-20,404, 1995.

Solomatov, S., and D. J. Stevenson, Can sharp seismic discontinuities be caused by non-equilibrium phase transformations?, *Earth Planet. Sci. Lett.*, *125*, 267-279, 1994.

Stammler, K., R. Kind, N. Petersen, G. Kosarev, L. Vinnik and L. Qiyan, The upper mantle discontinuities: Correlated or anti-correlated?, *Geophys. Res. Lett.*, *19*, 1563-1566, 1992.

Tarantola, A., *Inverse Problem Theory: Methods for data fitting and model parameter estimation*, 613 pp., Elsevier Sci., New York, 1987.

Van der Lee, S., and G. Nolet, Seismic image of the subducted trailing fragments of the Farallon plate, *Nature*, *386*, 266-269, 1997.

Van der Lee, S., H. Paulssen, and G. Nolet, Variability of *P660s* phases as a consequence of topography of the 660 km discontinuity, *Phys. Earth Planet. Int.*, *86*, 147-164, 1994.

Vinnik, L. P., Detection of waves converted from *P* to *SV* in the mantle, *Phys. Earth Planet. Inter.*, *15*, 39-45, 1977.

Vinnik, L. P., R. A. Avetisjan, and N. G. Mikhailova, Heterogeneities in the mantle transition zone from observations of *P*-to-*SV* converted waves, *Phys. Earth Planet. Inter.*, *33*, 149-163, 1983.

Vinnik, L. P., G. Kosarev, and N. Petersen, Mantle transition zone beneath Eurasia, *Geophys. Res. Lett.*, 23, 1485-1488, 1996.

Wood, B. J., The effect of H_2O on the 410-kilometer seismic discontinuity, *Science*, *268*, 74-76, 1995.

K. G. Dueker and A. F. Sheehan, Campus Box 399, Department of Geological Sciences, University of Colorado, Boulder, CO 80309. (e-mail: ken@mantle.colorado.edu)

(Received November 21, 1996; revised September 27, 1997; accepted November 24, 1997.)